LAWRENCE
LIVERMORE
NATIONAL
LABORATORY

LLNL-JRNL-412964

Material removal and surface figure during pad polishing of fused silica

T. I. Suratwala, M. D. Feit, W. A. Steele

May 12, 2009

Journal of American Ceramic Society

Disclaimer

Last Revision: 5/1/09

Material removal and surface figure during pad polishing of fused silica

Tayyab I. Suratwala, Michael D. Feit, William A. Steele
Lawrence Livermore National Laboratory, P.O. Box 808, Livermore, CA 94551, USA
suratwala1@llnl.gov

Abstract

The material removal and surface figure after ceria pad polishing of fused silica glass have been measured and analyzed as a function of kinematics, loading conditions, and polishing time. Also, the friction at the workpiece/lap interface, the slope of the workpiece relative to the lap plane, and lap viscoelastic properties have been measured and correlated to material removal. The results show that the relative velocity between the workpiece & lap (determined by the kinematics) and the pressure distribution determine the spatial and temporal material removal and hence the final surface figure of the workpiece. In the case where the applied loading and relative velocity distribution over the workpiece are spatially uniform, a significant non-uniform spatial material removal from the workpiece surface is observed. This is due to a non-uniform pressure distribution resulting from: 1) a moment caused by a pivot point and interface friction forces; 2) viscoelastic relaxation of the polyurethane lap; and 3) a physical workpiece/lap interface mismatch. Both the kinematics and these contributions to the pressure distribution are quantitatively described, and then combined to form a spatial and temporal Preston model & code for material removal (called Surface Figure or SurF©). The surface figure simulations are consistent with the experiment for a wide variety of polishing conditions. This study is an important step towards deterministic full-aperture polishing, which would allow optical glass fabrication to be performed in a more repeatable, less iterative, and hence more economical manner.

1. Introduction

A typical optical fabrication process involves a series of basic process steps including: 1) shaping, 2) grinding, 3) polishing, and sometimes 4) sub-aperture tool polishing. With significant innovation and development over the years in both shaping using computer numerical controlled (CNC) grinding machines and sub-aperture polishing using, for example, magneto-rheological finishing (MRF), these processes have become more deterministic. However, full aperture or conventional polishing still relies heavily on the optician's insight to get to the desired surface figure and is far from reaching the label of a deterministic process. Conventional polishing often requires multiple

iterative cycles involving polishing, measuring the surface figure, and adjusting the polishing parameters to converge to the desired surface figure (i.e., flatness or radius). Developing a scientific and quantitative understanding of the material removal during conventional polishing would lead to a process that is more determinisitic, allowing optical glass fabrication to be performed in a more repeatable, less iterative, and more economical manner. This is the motivation of the current study.

At the molecular level, material removal during glass polishing is dominated by chemical processes [1]. The most common polishing media for silica glass is cerium oxide which has the following the basic reaction:

$$\text{=Ce-OH} \quad + \quad \text{HO-Si}\equiv \quad \rightarrow \text{=Ce-O-Si}\equiv + H_2O \tag{1}$$

where the surface of the cerium oxide particle is cerium hydroxide which condenses with the glass surface (silanol surface) to form a Ce-O-Si bond. The bond strength of this new oxide is greater than the strength of the Si-O-Si bond (i.e., the glass). Hence the ceria particle essentially tears away individual silica molecules. Parameters such as pH, isoelectric point, water interactions, slurry concentration, slurry particle size distribution, and other chemical parameters can influence the removal rate [1].

At the macroscopic level, material removal has been historically described by the widely used Preston's equation [2-3]:

$$\frac{dh}{dt} = k_p \, \sigma_o \, V_r \tag{2}$$

where dh/dt is the average thickness removal rate, σ_o is the applied pressure, and V_r is the average relative velocity of the polishing particle relative to the substrate. The molecular level effects are described macroscopically by the Preston's constant (k_p). The rate of removal increases linearly with pressure and velocity. Many studies, particularly those in the chemical mechanical polishing (CMP) literature for Si wafer polishing, have expanded the Preston model to account for slurry fluid flow and hydrodynamic effects [4-9], Hertzian contact mechanics [1], influence of asperity microcontact [10-12], lap bending [13], and the mechanics of contact on the pressure distribution [14-16]. Only a few of these studies focus on understanding & predicting surface figure (or global non-uniformity), and none of these can yet be applied to the general case where all of these phenomena described above play a role.

In the following study, material removal and surface figure are measured for the fused silica glass that has been polished using a cerium oxide slurry on a polyurethane lap under a systematic set of polishing conditions. A spatial and temporal Preston model is formulated and used to simulate the experimental data incorporating: 1) the friction coefficient as function of velocity (Stribeck curve),

2) the relative velocity which is determined by the kinematics of the lap and workpiece motions, and 3) the pressure distribution which is shown to be dominated by: a) moment forces, b) lap viscoelasticity; and c) workpiece/lap interface mismatch.

2. Experimental

2.1. Polishing and Surface Figure Measurements

Silica glass disks (Corning 7980; 100 mm in diameter x 10 mm thick; polished by Sydor Optics to a Peak-to-Valley <0.3 μm) were re-polished on an orbital polisher in a configuration shown schematically in Fig. 1a. Before polishing, a polyurethane lap (SUBA 550 2.2 mm thick with square patterned grooves (2 mm width, 10 mm spacings)) on an aluminum base plate (200 or 300 mm in diameter x 50 mm thick) was preconditioned using a CMP diamond conditioner (Diamonex 250355FT) with a micro-90 soap solution. Also, an Al disk (76 mm diameter) was normally mounted on the back face of the workpiece glass using wax (Pitchbar holding wax PB7575), and a load (P) was applied by weights on a steel driving pin (9.5 mm diameter). The only exceptions are for Samples E2 & E3 (see Table 1) where the workpiece was guided by wheels at three points on the edge (hence no load driving pin was used). Cerium oxide slurry (Hastilite PO; ~0.5 μm particle size; diluted to Baume 9) was magnetically stirred externally and fed onto the lap using a peristaltic pump (Masterflex L/S) at a flow rate of 0.6 ml/minute. The kinematic controls on the orbital polisher include the rotation rate of the lap (R_L), separation distance between the workpiece center and lap center (s), stroke rate (R_s), and stroke distance (d_s) (see Fig. 1b). Note the rotation of the workpiece (R_o) in these experiments was not controlled, but was driven by the friction caused by the lap and stroke motion. In some of the polishing experiments (Samples F1 & F2) an external glass septum (152 mm OD, 105 mm ID, 9.5 mm thick) was loaded by weights (P_s) onto the pad around the fused silica workpiece which also freely rotated with the workpiece.

The glass samples were polished under various conditions (as described in Table 1) and then periodically removed and cleaned with water (note the wax and Al button were removed and reapplied after each iteration). The weight of the workpiece (±0.001 gms) and the reflected wavefront of the polished face (using a Michelson Interferometer, 4" ADI Phaseshift MiniFiz 100) were measured after each polishing iteration.

2.2 Friction Measurements

The friction between the workpiece and the lap was measured as a function of lap rotation (R_L) and applied load (P) using a setup schematically shown in Fig. 2a. A rectangular fused silica glass workpiece (37.5 mm x 7.8 mm x 10 mm) waxed onto an Al disk was polished on the 37.5 x 7.8 mm face of the sample with the spacing between the lap and sample center of 120 mm. A calibrated

load cell (Interface WMC-25, 0-25 lbf), which wasattached to the side of the Al disk and fixed against a stationary surface, directly measured the friction force in tension.

2.3 Workpiece slope measurements

The tilt or slope of the workpiece relative to the lap plane was measured during polishing using a setup schematically shown in Fig. 2b. Two laser displacement sensors (Keyence Models LK-G37 & LK-G32) were placed on two fixed points above the workpiece (one near the leading edge of the workpiece and one near the trailing edge of the workpiece). The height difference between the displacement sensors, initially zeroed on the workpiece while stationary and unloaded, was measured as a function of moment arm distance (d), applied load (P), and lap rotation rate (R_L). Because the lap was not co-planar (i.e., it wobbles slightly relative to its center of rotation axis) and was not perfectly parallel to the machine plane, the tilt of the workpiece was determined using the measured height difference in the forward and reverse lap rotation. The workpiece tilt (ΔH) and slope angle (θ_x) are:

$$\Delta H = \frac{\Delta H_f - \Delta H_r}{2} \tag{3a}$$

$$\theta_x = \arctan\left(\frac{\Delta H}{2r_o}\right) \tag{3b}$$

where ΔH_f and ΔH_r are the average measured height differences between the leading edge and the trailing edge for the lap rotating in the forward and reverse direction, respectively.

2.4 Lap viscoelastic properties

The viscoelastic properties of the polyurethane pad (Suba 550) were measured by compressively loading the lap at various pressures and measuring the displacement as a function of time in a configuration shown schematically in Fig. 2c. A mechanical test machine (Instron 1127) displaced a steel loading plate (89 mm in diameter) at a rate of 100 mm/min onto the polyurethane pad (100 mm in diameter) adhered to a flat steel plate. The non-axial motion of the weight stack was constrained by a linear ball bearing to maintain alignment. Also, a spherical seat was attached to the bottom flat steel plate to ensure parallel contact with the steel loading plate. Three positional sensors (Kaman 1SM, pre-calibrated, located on a 120 mm diameter circle around the lap, 120^o apart, ±0.1 μm) were used to measure the time dependent position, and a load cell (Interface 100 lbf, ±0.05 psi) was used to measure the time dependent load. Both the positional sensor and the load cell had a time response accuracy of ±1 msec.

3. Results

3.1 Surface Figure

When the workpiece was allowed to rotate during polishing, the measured surface figure was radially symmetric. Hence the surface can be fully represented by a radial lineout for each polishing time increment. After each polishing iteration, the mass of material removed (Δm) and the radial lineout ($L(x,t_i)$) at polishing time t_i were measured. From a simple volume balance, the height difference (Δh) between the two lineouts measured at different polishing times (t_1 and t_2) is then:

$$\Delta h = \frac{\frac{\Delta m}{\rho} - \int_0^{r_o} (L(x,t_1) - L(x,t_2))\, 2\pi\, x\, dx}{\pi\, r_o^{\,2}} \tag{4}$$

where ρ is the density of fused silica (2.2 gm/cm^3) and r_o is the radius of the workpiece. The measured profiles for each time increment can now all be plotted relative to the original starting surface. The surface figures for each of the polishing experiments listed in Table 1 are plotted in this format in Figures 3-9.

3.2 Workpiece slope

The measured workpiece tilt and slope angle as a function of various polishing conditions (moment arm distance (d), applied pressure (σ_o), and lap rotation rate (R_L)) are plotted in Fig. 10. The tilt ranged from 0 - 35 μm or 0 - 0.19x10^{-3} deg. Note that a positive tilt height or slope angle indicates that the leading edge is lower than the trailing edge. The tilt was largely unaffected by lap rotation, but increased with the moment arm distance and applied pressure.

3.3 Lap creep compliance

Fig. 11a shows an example of the data collected from pad loading experiments described in Section 2.4; the measured load (plotted in terms of pressure on the workpiece) and the displacement of the pad as a function of time are shown for the case where the applied pressure was 0.3 psi. In order to characterize the viscoelastic nature of the pad, the pad relaxation rate under constant loading is needed (referred to as the creep compliance time constant (τ_c)). Since the loading time was not instantaneous (~0.08 sec), the pad relaxation was evaluated by fitting the displacement data to a single exponential after full loading was achieved (see Fig. 11b). For loading conditions ranging from 1 -3 psi, reasonable fits are obtained with a similar creep compliance time constant of 4.0±0.1 sec. This value is utilized further in the viscoelastic model described in Section 4.3.2.

4. Discussion

In order to quantitatively simulate the surface figure evolution during polishing, Preston's model (Eq. 1) for material removal needs to be expanded to account for numerous effects such as: 1) spatial and temporal variation in velocity and pressure; 2) differences in the applied pressure and

pressure distribution experienced by the workpiece; and 3) friction effects. Hence, a more elaborate form of Preston's Equation can be described as:

$$\frac{dh_i}{dt}(x,y,t) = k_p\ \mu(v_r(x,y,t))\ \sigma(x,y,z,t)\ v_r(x,y,t) \tag{5a}$$

$$\frac{dh}{dt}(x,y,t) = \frac{k_p}{t}\int_0^t \mu(v_r(x,y,t'))\ \sigma(x,y,z,t')\ v_r(x,y,t')\ dt' \tag{5b}$$

where dh_i/dt & dh/dt are the instantaneous & time average removal rates, respectively, at some given time t and position x,y on the workpiece. μ is the friction coefficient which is a function of the relative velocity (v_r) at the workpiece/lap interface. σ is the pressure distribution resulting from the applied pressure (σ_o) and the nature of the workpiece/lap contact. In the discussion that follows, three critical components of the modified Preston's equation (Eq. 5a) are described: 1) the frictional forces as function of relative velocity between the polishing particle and workpiece; 2) the relative velocity between the workpiece and lap based on various kinematics; 3) the factors that affect the pressure distribution (moment forces & workpiece tilt, lap viscoelasticity, and workpiece/lap interface mismatch). All of these effects are combined to form a more global material removal model and its implications are discussed below.

4.1 Frictional forces

The contribution of interface friction to material removal (see Eq. 5a) can conceptually be thought of as being proportional to the number of polishing particles making contact with the workpiece. The greater the number of particles making contact, the greater the friction, and the greater the removal rate. As discussed in Section 2.2, the friction force (F) was measured as a function of applied load (P) and lap rotation rate (R_L). The friction coefficient for each measurement is then:

$$\mu = \frac{F}{P}\ . \tag{6}$$

The magnitude of the friction between the workpiece and the lap is determined by the mode of contact between the two bodies, the applied load, the characteristics of the slurry (e.g. viscosity), and the workpiece/lap relative velocity [4-5]. It is common to describe the dynamic friction using the Stribeck Curve (μ as function of $\frac{\eta_s v_r}{\sigma_o}$ where η_s is the slurry fluid viscosity) as shown in Fig. 12 [4]. Notice that the friction coefficient can change significantly depending on the velocity and applied pressure. At low values of $\frac{\eta_s v_r}{\sigma_o}$ ($<10^{-6}$ m) for the pad, the workpiece and lap make mechanical contact (referred to as contact mode), and the friction coefficient is high (0.7 – 0.8); at high values of $\frac{\eta_s v_r}{\sigma_o}$ ($>10^{-5}$ m), the fluid pressure of the slurry carries the workpiece off of the lap (referred to as hydrodynamic mode), and the friction coefficient is low (<0.02). Most conventional

optic polishing is performed in contact mode, where the friction coefficient is large and does not significantly change. Notice in Fig. 12 that the polyurethane pad, pitch and IC1000 pad follow the same basic behavior with the friction coefficient on the Stribeck curve. However, the transition into hydrodynamic mode occurs at different values of $\frac{\eta_s v_r}{\sigma_o}$ depending on the properties of the lap material. For the polyurethane pad, the friction cofficient can be described by a sigmoidal curve, which is often used to describe the shape of the Stribeck curve, as:

$$\mu = 0.7 - \frac{0.6}{1 + \left(7.7 \times 10^4 m^{-1} \frac{\eta_s v_r}{\sigma_o} \right)^{0.9}} \quad . \tag{7}$$

4.2 Kinematics and relative velocity

Another major contributor to material removal is the relative velocity of the polishing particle to the workpiece surface (Eq. 5a). The greater the velocity of the polishing particle, the larger the number of particles that will interact with the surface per unit time, thus leading to greater material removal. Kinematic analysis for various polishing scenarios has been previously summarized (for example see Brown [17] and Taylor [18]). Assuming that the workpiece-particle relative velocity is roughly equivalent to the workpiece-lap relative velocity (i.e., the polishing particle is essentially stationary relative to the lap), the kinematic parameters of the system can be used to calculate the relative velocity of the polishing particles. It is convenient to describe the relative velocity in vector form as:

$$\vec{v}_r(x,y,t) = \left(\vec{R}_o \times \vec{\rho}_o(x,y,t)\right) - \left(\vec{R}_L \times \left(\vec{\rho}_o(x,y,t) - \vec{S}(t)\right)\right) + \frac{d\vec{S}(t)}{dt} \tag{8}$$

where ρ_o is a position on the workpiece given by coordinates x & y with the origin at the workpiece center, $\vec{R}_o$ & $\vec{R}_L$ are the rotation rates of the workpiece and lap in vector form directed along the z-axis, and $\vec{S}$ is the vector describing the separation between the geometric centers of the workpiece and lap. The first term on the right hand side describes the rotation velocity of the workpiece for some given position on the workpiece at the workpiece-center frame of reference. The second term describes the rotation velocity of the lap at the workpiece-center frame of reference. The final term describes the linear motion relative velocity due to the stroke. For the case of spindle polishing used in this study, each of the terms above can be described in vector form using:

$$\vec{R}_o = \begin{pmatrix} 0 \\ 0 \\ R_o \end{pmatrix} \quad \vec{R}_L = \begin{pmatrix} 0 \\ 0 \\ R_L \end{pmatrix} \quad \vec{S} = \begin{pmatrix} d_s \sin(R_s t) \\ s \\ 0 \end{pmatrix} \quad \vec{\rho}_o = \begin{pmatrix} \sqrt{x^2 + y^2} \sin\left(\arctan(x/y) + 2\pi R_o t\right) \\ \sqrt{x^2 + y^2} \cos\left(\arctan(x/y) + 2\pi R_o t\right) \\ 0 \end{pmatrix} \tag{9a-d}$$

In order to describe a typical continuous polisher (CP), one just needs to set d_s equal to 0.

Since the relative velocity can only lead to removal when the lap and workpiece are in contact, an additional condition for a non-zero relative velocity applies for the case of a circular lap:

$$\left|\vec{\rho}_o(x,y,t) - \vec{S}(t)\right| \le r_L \ . \tag{9}$$

The time average relative velocity is then given by:

$$V_r(x,y) = \frac{1}{t}\int_0^t \vec{v}_r(x,y,t')\,dt' \ . \tag{10}$$

Using Eqs. 8-10, the time average velocity has been calculated for a variety of kinematics in Figure 13 where r_o=0.05 m, r_L=0.10 m, R_L=28 rpm. When V_r is higher on the edge relative to the center, the workpiece would become more convex, and when V_r is lower on the edges, the workpiece would become more concave. Fig 13a suggests that as the workpiece rotation rate is mismatched from the lap rotation rate, the workpiece would become more convex. Figs. 13a&b suggest that increasing the separation distance, tends to increase the time average velocity and hence removal rate. Figs. 13c&d illustrate that increasing the stroke distance generally leads to lower velocities at the edge due to the edges of the workpiece spending more time off of the lap, and hence the workpiece would become more concave. These trends are consistent with those generally observed by opticians during conventional polishing.

4.3 Pressure Distribution

The pressure distribution between the workpiece and lap is more complex and not as well understood due to the multiple factors that can affect it. Figure 14 schematically shows some of the phenomena that can influence the pressure distribution; these include: 1) the distribution of pressure applied onto the workpiece or lap, 2) the elastic response of the lap (including the rigid punch effect and workpiece/lap deflection), 3) the hydrodynamic forces due to fluid flow at the interface, 4) the moment resulting from the moment arm distance and frictional forces, 5) the viscoelastic relaxation of the lap, and 6) the physical mismatch at the workpiece/lap interface.

It is common for optical manufacturers to purposely modify the distribution of the applied load in order to alter the removal on a certain portion of the workpiece. For this study, only uniform loading is examined in order to understand the contribution of the other phenomena listed above.

The elastic response of the lap can lead to a non-uniform pressure distribution due to the change in response of the lap at the edge of the workpiece/lap interface. This effect has been described previously (see for example [19]) having the following form for the 1D pressure distribution as:

$$\sigma(x) = \frac{P}{\pi\left(R^2 - x^2\right)^{1/2}} \ . \tag{11}$$

This results in a pressure distribution that is high at the edge of the workpiece. However, the shape of this pressure distribution alone cannot account for the measured material removal and surface figure. Another elastic contribution to the pressure distribution is the deflection of both the workpiece and lap. Such effects can be quantified using finite element analysis or estimated using standard equations for deflection and stress [20]. The polishing setup used in this study is one where both the workpiece and lap are stiff enough so that these effects are expected to be small and are not considered in the analysis of the experimental results.

Hydrodynamic effects can also influence the pressure distribution due to high fluid pressure passing through the workpiece/lap interface. These effects are described by the well known Reynolds equation [4,5,7,8,21]; in 1D it is described as:

$$\frac{d(\sigma(x))}{dx} = -6\eta_s V_r \frac{\Delta h_{oL}(x) - \Delta h_{oL}^*}{\Delta h_{oL}(x)^3} \tag{12}$$

where σ is the resulting pressure distribution, η_s is the fluid viscosity, Δh_{oL} is the gap between the workpiece and lap, Δh_{oL}^* is the gap at the point of maximum pressure on the workpiece. However, hydrodynamic effects are likely not the dominant effect on the pressure distribution for typical optical polishing. This is because optical polishing usually does not operate in hydrodynamic contact mode (see friction discussion above) where the removal rate would be very small (essentially non-existent). Also, hydrodynamic effects would cause the leading edge of the workpiece to be higher than the trailing edge relative to the lap plane which is inconsistent with the measured data as shown in Fig. 10.

Below is a detail description of the three other effects (moment forces, viscoelastic lap effects, and workpiece/lap mismatch) which tend to dominate the pressure distribution during optical polishing.

4.3.1 Influence of moment forces on pressure distribution

Several groups have acknowledged the potential impacts of slope of the workpiece during Si wafer polishing [8,21] driven by hydrodynamic forces. Here a moment force driven by the friction at the workpiece/lap interface while in contact mode is described. Consider the workpiece-lap setup as shown in Figure 2b where the workpiece is held by a spindle and allowed to rotate. Using a force and moment balance while at equilibrium, the total load and moment are given by:

$$P = \int_{optic} \sigma(x,y)\, dx\, dy \tag{12a}$$

$$M_x = \int_{optic} \sigma(x,y)\, y\, dx\, dy - F_y d = 0 \tag{12b}$$

$$M_y = F_x\, d - \int_{optic} \sigma(x,y)\, x\, dx\, dy = 0 \tag{12c}$$

where F_x & F_y are the friction force and M_x & M_y are the moment in the x & y direction.

From the results shown in Figure 10, a non-zero workpiece slope is clearly present during polishing. The slope increases (where the leading edge of the workpiece is lower than the trailing edge) with moment arm distance and applied pressure. This is qualitatively consistent with the above formalism, since it would result in higher pressure at the leading edge of the workpiece. The determination moment and slope using Eq. 12a-d becomes more complicated with the addition of stroke in the kinematics where the moment and hence slope become time dependent (i.e. slope changes with position of the workpiece along the stroke trajectory). Also, any offset of the workpiece from the lap surface changes the pressure distribution over a smaller area of the workpiece, and any offset of the workpiece from the lap surface can also lead to an additional slope due to a center of gravity balance. Due to the fact the above complications are not yet developed in the model, the slope is not predetermined but used as a fitting parameter in this study. The slope due to the moment combined with the viscoelastic lap contributions lead to a non-uniform pressure distribution as described in more detail in the next section.

4.3.2 Influence of viscoelastic lap properties on pressure distribution

With a moment distance of essentially zero (i.e., all moment forces removed), as with Sample E2 (see Fig. 6b), a non-uniform material removal is still observed. This leads to isolation of another source of non-uniform pressure distribution that is believed to be caused by viscoelastic lap relaxation. The influence of the viscoelastic properties of this polyurethane lap has been previously correlated to the length of scratches caused by rogue particles viscoelastically penetrating into the lap [22]. With a viscoelastic lap, the pressure at the leading edge (when a point on the lap first makes contact with the workpiece) of the workpiece is higher than at the trailing edge (when a point on the lap stops making contact with the workpiece). This is because as a given point on the lap travels through the workpiece interface, the lap material has a time dependent relaxation (i.e., with time, the lap relaxes and reduces the pressure on the workpiece).

For a viscoelastic lap loaded by an elastic workpiece, the pressure distribution on the workpiece ($\sigma(x,y)$) can be described by the heredity equation for a constant applied load as [19]:

$$\sigma(x,y) = \int_o^{t_L(x,y)} E_{rel}\left(t_L(x,y) - t'\right)\dot{\varepsilon}(t')\,dt' \tag{13}$$

where $t_L(x,y)$ is the time of lap exposure at some point x,y on the workpiece for the corresponding point on the lap, E_{rel} is the stress relaxation function for the viscoelastic lap material, and $\dot{\varepsilon}(t')$ is the lap strain rate. Each of these three parameters is analytically described below.

The time of lap exposure can be determined using a line path of some point on the lap (x_L,y_L) at the leading edge of the workpiece as it travels to some given point on the workpiece (x,y) as illustrated in the schematic in Fig. 15a. For the case of kinematics without stroke, the time of lap exposure is given by:

$$t_L(x,y) = \frac{1}{R_L}\arccos\left(\frac{x \cdot x_L(x,y) + (y+s)(y_L(x,y)+s)}{x^2 + (y+s)^2}\right) \tag{14a}$$

where:

$$y_L(x,y) = \frac{x^2 + (y+s)^2 - r_o^{\,2} - s^2}{2s} \tag{14b}$$

$$x_L(x,y) = \sqrt{r_o^2 - y_L(x,y)^2}\ . \tag{14c}$$

Note for every point selected on the workpiece (x,y), there is a unique corresponding point at the leading edge of the workpiece (x_L,y_L). Figure 15b plots the calculated time of lap exposure $t_L(x,y)$ for the conditions used for Sample A1 using Eq. 14a-c. The minimum time of lap exposure is at the leading edge of the workpiece and the maximum time of exposure is at the trailing edge on the side of the workpiece closest to the lap center. The asymmetry of the time of lap exposure is due to the fact that the velocity of a given point on the lap is lower closest to the lap center, which leads to longer times of lap exposure. For the case shown in Fig. 15b, the maximum time of lap exposure is 0.6 sec. A similar exercise, as described above, can be performed for the case with stroke added; however, the algebra is more complicated. Also, the time of lap exposure would change along the stroke cycle, whereas without stroke the time of lap exposure stays constant.

The viscoelastic lap behavior can be modeled using the delayed elasticity viscosity model [19]; Fig. 16 schematically illustrates this model which is comprised of two moduli (two springs) and one viscosity (dashpot). The creep compliance function J(t) and the stress relaxation function $E_{rel}(t)$ for this model are described as [19]:

$$J(t) = \frac{1}{E_1} + \frac{1}{E_2}\left(1 - e^{\frac{-t}{\tau_c}}\right) \qquad E_{rel}(t) = \frac{E_1}{E_1 + E_2}\left(E_2 + E_1 e^{\frac{-t}{\tau_s}}\right) \tag{15a-b}$$

where τ_c is the creep compliance time constant and τ_s is the stress relaxation time constant. For this model the following self similar relationships apply [19]:

$$E_1 + E_2 = E \qquad E_2 = \frac{\eta}{\tau_c} \qquad \tau_s = \frac{\eta}{E} \tag{15c-e}$$

where E and η are the bulk modulus and viscosity of the lap. This simple viscoelastic model (delayed elasticity model) is one possible viscoelastic model; that is not to say that a more complex, possibly more realistic model can also be implemented.

From the results described in Section 3.3, τ_c=4.0 sec. From dynamic mechanical analysis performed by Lu et. al. [23] on this polyurethane pad, E= 100 MPa and $\eta = 9.7\times10^7$ poise. Hence using Eqs 15c-e, E_1=97.75 MPa, E_2=2.25 MPa and τ_s=0.1 sec. Note that the stress relaxation time constant (τ_s) is less than the maximum time of lap exposure (see Fig. 15b), suggesting that a significant amount of stress relaxation can occur under these set of kinematics with this pad. With all of these parameters quantitatively known, the stress relaxation function (Eq. 15b) is now quantitatively defined.

The final component needed to determine the pressure distribution (using Eq. 13) due to viscoelastic relaxation is the strain rate ($\dot{\varepsilon}(t')$). The strain on the lap is constrained by the shape of the workpiece and its orientation with respect to the lap (i.e., the slope). For the cases where the workpiece surface is flat, the strain as a function of workpiece position can then be defined as:

$$\varepsilon(x,y) = \frac{\tan(\theta_x)\,x}{t_{pad}} + \frac{\tan(\theta_y)\,y}{t_{pad}} + \varepsilon_o \tag{16}$$

where θ_x and θ_y are the slopes of the workpiece in the x and y directions relative to the lap plane, ε_o is the elastic strain at the center of the workpiece, and t_{pad} is the thickness of the viscoelastic pad. It is convenient to describe the strain as a function of time ($\varepsilon(t)$) instead of position, which can be done using:

$$x = r_{arc}\cos\left(R_L t + \left(\arccos\frac{x_L}{r_{arc}}\right)\right) \qquad y = r_{arc}\sin\left(R_L t + \left(\arccos\frac{x_L}{r_{arc}}\right)\right) - s \tag{17a-b}$$

$$r_{arc} = \sqrt{x^2 + (y+s)^2} \tag{17c}$$

where r_{arc} is the arc radius for a given point (x_L, y_L) at the leading edge of workpiece (see Figure 15a) relative to the lap center. Substituting into Eq. 16 and then differentiating, gives the strain rate as:

$$\dot{\varepsilon}(t) = -\frac{\tan(\theta_x)}{t_{pad}} r_{arc}\sin\left(R_L t + \left(\arccos\frac{x_L}{r_{arc}}\right)\right) - \frac{\tan(\theta_y)}{t_{pad}} r_{arc}\cos\left(R_L t + \left(\arccos\frac{x_L}{r_{arc}}\right)\right) \quad . \tag{18}$$

Using Eqs. 13-18, one can now determine the pressure distribution on a non-rotated workpiece. Figure 17a shows the calculated pressure distribution using the conditions described for Sample B where the workpiece does not rotate. For comparison, the measured surface profile for Sample B after 1 hour of polishing is shown in Fig. 17b. Note the leading edge of workpiece in each image is designated by a red star. The observed removal is qualitatively consistent with the calculated pressure distribution where the leading edge experiences a much higher removal or pressure. For all of the other samples in this study, the workpiece was rotated. Hence the pressure distribution would

be a time-average of non-rotated pressure distribution rotated about the center of the workpiece, which can be described as:

$$\sigma(r) = \frac{1}{2\pi}\int_0^{2\pi} \sigma(r,\theta)\, d\theta \tag{19}$$

where $\sigma(r,\theta)$ is the pressure distribution determined by Eq. 13 in cylindrical coordinates. As the slope of the workpiece is increased relative to the lap plane, in Eq. 18, the time average rotated pressure distribution becomes more non-uniform and hence the material removal becomes more non- uniform.

4.3.3 Influence of workpiece/lap mismatch on the pressure distribution

Another strong influence on the pressure distribution is the surface mismatch of the workpiece/lap interface. If both surfaces are perfectly matched, then the mismatch is zero and the pressure distribution is uniform (if we ignore other effects contributing to the pressure distribution). If the surfaces are not matched, the pressure distribution will not be uniform leading to lower pressures where the mismatch is larger and higher pressures where the mismatch is small. The compliance of the workpiece and lap would influence the magnitude of the pressure deviation. Another way of describing the mismatch effect is using a nonlinear strain and strain rate; in the previous section, a linear strain analysis was described.

To illustrate the mismatch effect quantitatively for the polyurethane pad used in this study, we compare two series of polishing experiments performed on a flat lap Al base (±1 μm peak to valley) (Samples A1 & C1) with those performed on a convex lap Al base (±20 μm peak to valley) (Samples D5 & D1). The surface figure lineouts for each of these can be found in Figs 3, 4, 5 & 7. The average measured removal rates for these samples are shown in Figs. 18 a&b. Each plot only compares samples that were performed under identical polishing conditions except for the curvature of the lap Al base. The removal rate using the convex lap was greater at the center of the workpiece and lower at the edges of the workpiece relative to the removal rate observed using the flat lap. This deviation in removal is due to the change in pressure distribution due to the workpiece/lap mismatch. Taking the ratio of the removal rate at each radial position for each of the two series of samples in Figs. 18 a&b, the relative removal as a function of radial position on the workpiece is shown in Fig. 18c. Note that the effect of lap curvature on the removal for both series of polishing experiments was about the same even though they were conducted under very different kinematics. For both series of polishing experiments, the removal rate decreased by 50% at the edge relative to the removal rate at the center of the workpiece.

The relative removal shown in Fig. 18c can now be described in terms of the workpiece/lap mismatch by describing the lap curvature as a sphere. The height ($h_L(x)$) of the lap normalized to zero at the ends is given by:

$$h_L(x) = \sqrt{\rho_L^{\,2} - x^2} - (\rho_L - h_{PV}) \tag{20}$$

where ρ_L is the radius of curvature of the lap surface and h_{PV} is the peak to valley height of the lap. For the convex lap used here, ρ_L is 250 m and h_{PV}= 20 μm.

Allowing the workpiece to tilt to achieve best contact with the lap, we get the mismatch between the workpiece and the lap as:

$$\Delta h_{oL}(x) = h_L(x) - h_o(x) \tag{21}$$

where the $h_o(x)$ is the height of the workpiece described by:

$$h_o(x) = \tan(\theta_x)x + h_i \tag{22}$$

where h_i is height at the center of the workpiece. For the convex lap used here, $\tan(\theta_x)$ =20 μm/100 mm=2x10^{-4} and h_i= 20 μm. Applying Eqs. 20-22, the data in Fig. 18c was converted to the relative pressure as a function of the workpiece/lap mismatch in Fig. 18d. The data shows that a removal rate (and hence pressure) on the workpiece drops linearly; at a 5 μm mismatch, the pressure and removal drop ~50%. The belief is, however, for larger amounts of mismatch, the pressure dependence on the mismatch would become nonlinear. Hence, the relative pressure as a function of mismatch $\Delta h_{oL}(x))$ is quantitatively described as:

$$\frac{\sigma}{\sigma_o}(\Delta h_{oL}) = e^{-\Delta h_{oL}/\bar{h}} \tag{23}$$

where $\bar{h}$ is a constant describing the rate at which pressure drops with increase in workpiece/lap mismatch. A reasonable fit to the data is obtained using $\bar{h}$ = 8 μm which is shown as a solid line in Fig. 18d. The workpiece/lap mismatch calibration to the pressure distribution can now be used to monitor the pressure distribution (Eq. 23) as a function of polishing time which is discussed in greater detail in the next section.

4.4 Time varying quantities and achieving & predicting convergence

For the polishing system used in this study (i.e. pad polishing on an Al base), the relative wear of the pad is considered small and negligible relative to the workpiece wear. Hence, during polishing, the workpiece should converge to a certain shape where the pressure non-uniformity caused by the workpiece/lap mismatch is balanced by the pressure non-uniformity due to other effects outlined in Fig. 14. To illustrate this, consider Samples D5 and E2 whose results have been replotted in terms of PV height of the surface figure as a function of polishing time (see Fig. 19). For both sets of polishing conditions, the figure is observed to converge with polishing time. If the pressure

distribution and time average velocity were not time varying, the PV height would continue to increase linearly and indefinitely. However, as discussed in the previous section, as the workpiece/lap mismatch is increased, the pressure distribution will change leading to a more uniform distribution of material removal and hence convergence of the surface figure with polishing time. Using the pressure versus mismatch curve shown in Fig. 18d and Eq. 23, a time dependent pressure distribution has been calculated to determine the surface figure and PV height (designated by the solid lines in Fig. 19). The use of the measured mismatch pressure dependence does a good job of predicting the change in the PV height with polishing time and the convergence value of the PV height.

4.5 Method for achieving uniform removal

A novel method to minimize the moment and viscoelastic effect on pressure non-uniformity is to use a septum on the exterior of the workpiece and load it sufficiently so that it prestrains the lap. Hence when the lap makes contact with the workpiece, the lap behaves elastically instead of viscoelastically. Samples F1 & F2 clearly show that use of a septum with high loads leads to very uniform removal (implying a uniform pressure distribution) (see Figs. 9 a & b). Note that the pressure on the septum ~3x that of the workpiece pressure was required to achieve this effect. This technique has the practical application of removing material from a workpiece without significantly changing its surface figure.

4.6 Deterministic Surface Figure Model (SurF©)

By combining all of the effects discussed above into the spatial and temporal dependent Preston's Equation (Eq. 5a), a finite difference, material removal model code (Surface Figure (SurF©)) has been written to incrementally calculate material removal (and hence surface figure) on every position of the workpiece and lap as a function of time. These effects include: 1) friction coefficient as function of velocity (Section 4.1); 2) velocity distribution as a function of position (Section 4.2); 3) moment contribution to the pressure distribution (Section 4.3.1); 4) viscoelastic lap contribution to the pressure distribution (Section 4.3.2); and 5) workpiece/lap mismatch contribution to the pressure distribution (Section 4.3.3). The four major terms of Eq. 5a (Preston's constant, relative velocity, friction coefficient, and pressure distribution) are treated as independent variables. The model has inputs of kinematics (R_o, R_L, d_s, R_s), configuration (r_o, r_L, shape, ρ_L, P), and material properties (η, k_p, stribeck curve (Eq. 7), mismatch response (Eq. 23)).

In this study, different polishing experiments were performed as described in Table 1 and plotted in Figs. 3-9. The key process variables include change in kinematics, change in loading conditions, change in the lap flatness, and the use of an external septum. The simulation or model results are plotted along with the data in Figs. 3-9 as dashed lines. In general, the simulation does a good job at quantitatively describing the shape of the workpiece surface as a function of time for a wide variety of process conditions while incorporating multiple effects of friction, kinematics, and multiple sources of pressure non-uniformity. The adjustable parameters used in the current model were the Preston's constant (k_p) and the slope (θ_x) on the workpiece for a given loading condition and kinematics. k_p changed very little from run to run except in the case where the loading conditions were significantly changed (see Table 1 last column). Also, the best fit values of k_p is consistent with values previously reported for ceria used on polyurethane pad [24]. θ_x varied both with kinematics and with moment arm distance. For the polishing runs conducted without stroke, the values of the slope (see Table 1 second last column) determined from the best fit follow the same trend as the slope measured directly (Fig. 10). Future work will focus on predicting the slope (eliminating it as a fitting parameter) and hence leading to a truly deterministic model for predicting material removal and surface figure during polishing.

5.0 CONCLUSIONS

The material removal and surface figure of fused silica glass after polishing (using ceria slurry on a polyurethane lap) has been measured and analyzed as a function of kinematics, loading conditions, and polishing time. Adding the quantitative effects of friction, kinematics (relative velocity), and multiple sources on pressure distribution, a more global model has been developed to understand the spatial and temporal dependence of material removal during full aperture polishing of fused silica. This study is an important step for achieving deterministic full-aperture polishing, which would allow optical glass fabrication to be performed in a more repeatable, less iterative, and hence more economical manner.

6.0 ACKNOWLEDGEMENTS

Work performed under the auspices of the US Department of Energy by Lawrence Livermore National Laboratory under contract DE-AC52-07NA27344 under the LDRD program. The author would like to thank Mary Leblanc for developing a setup for and measuring the viscoelastic properties of the lap material.

REFERENCES

[1] L. Cook, "Chemical processes in glass polishing", Journal of Non-Crystalline Solids 120 (1990) 152-171.

[2] N. J. Brown, “A short course in optical fabrication technology”, Optical Society of America Annual Meeting (1981), LLNL Preprint, UCRL-86796.
[3] F. Preston, Trans Opt. Soc. 23 (3) (1922) 141.
[4] I.M. Hutchings, “Tribology: Friction and Wear of Engineering Materials”, Butterworth/ Heinmann (1992).
[5] J. Lai, “Mechanics, Mechanisms, and Modeling of Chemical Mechanical Polishing Process”, Thesis MIT (2001).
[6] E. Terrell, C. Higgs, “Hydrodynamics of slurry flow in chemical mechanical polishing”, Journal of the Electrochemical Society 153 (6) K15-22 (2006).
[7] S. Runnels, L. Eyman, “Tribology Analysis of Chemical Mechanical Polishing”, Journal of the Electrochemical Society, 141 (6) (1994) 1698.
[8] S. Park, C. Cho, Y. Ahn, “Hydrodynamic analysis of chemical mechanical polishing process”, J. Tribology International 33 (2000) 723–730
[9] G. Nanz, L. Camilletti, “Modeling of Chemical Mechanical Polishing- A review”, IEEE Transactions on Semiconductor Manufacturing, 8 (4) (1995) 383.
[10] Y. Jeng, P. Huang, W. Pan, “Tribological Analysis of CMP with partial asperity contact”, Journal of the Electrochemical Society 150 (10) G630-637 (2003).
[11] Y. Jeng, P. Huang, “Impact of abrasive particles on the material removal rate”, Electrochemical and Solid State Letters 7 (2) G40-43 (2004).
[12] J. Lu, D. Dornfeld, “Material removal mechanism in chemical mechanical polishing” IEEE Transactions on Semiconductor Manufacturing, 14 (2) 112 (2001).
[13] S. Sivaram, H. Bath, E. Lee, R. Leggett, and R. Tolles, “Measurement and modeling of pattern sensitivity during chemical-mechanical polishing of interlevel dielectrics,” SEMATECH, Austin, TX, Tech. Rep.,1992.
[14] D. Wang, et. al. “Von Mises Stress in Chemical Mechanical Polishing Process” Journal of the Electrochemical Society 144 (3) 1191 (1997).
[15] T.-K. Yu, C. C. Yu, and M. Orlowski, “A statistical polishing pad modelfor chemical mechanical polishing,” in *IEDM Tech. Dig.,* 1993.
[16] Y. Li, “Microelectronic Applications of Chemical Mechanical Planarization”, John Wiley & Sons (2007).
[17] N. Brown, “Optical Fabrication”, LLNL Technical Report MISC 4476 (1989).
[18] J. Taylor, et. al. “High Speed Lapping of Flat Optics” UCRL-ID-119056 (Feb 1995) 4-13.
[19] K.L. Johnson, Contact Mechanics, Cambridge University Press (1985).
[20] R. Roark, W. Young, “Formulas for stress and strain”, McGraw-Hill, 5th edition (1982).
[21] E.J. Terrell and C. F. Higgs, “Hydrodynamics of Slurry Flow in Chemical Mechanical Polishing”, Journal of The Electrochemical Society, 153 6 K15-K22 (2006).
[22] T. Suratwala, R. Steele, M.D. Feit, L. Wong, P. Miller, J. Menapace, P. Davis, “Effect of rogue particles on the sub-surface damage of fused silica during grinding/polishing”, Journal of Non-Crystalline Solids 354 (2008) 2023–2037.
[23] H. Lu, Y. Obeng, K. Richardson , “Applicability of dynamic mechanical analysis for CMP polyurethane pad studies”, Materials Characterization, 49 (2003) 177.
[24] M. Cumbo, D. Fairhurst, S. Jacobs, B. Puchebner, “Slurry particle size evolution during the polishing of optical glass”, Applied Optics, 34 (19) (1995) 3743.

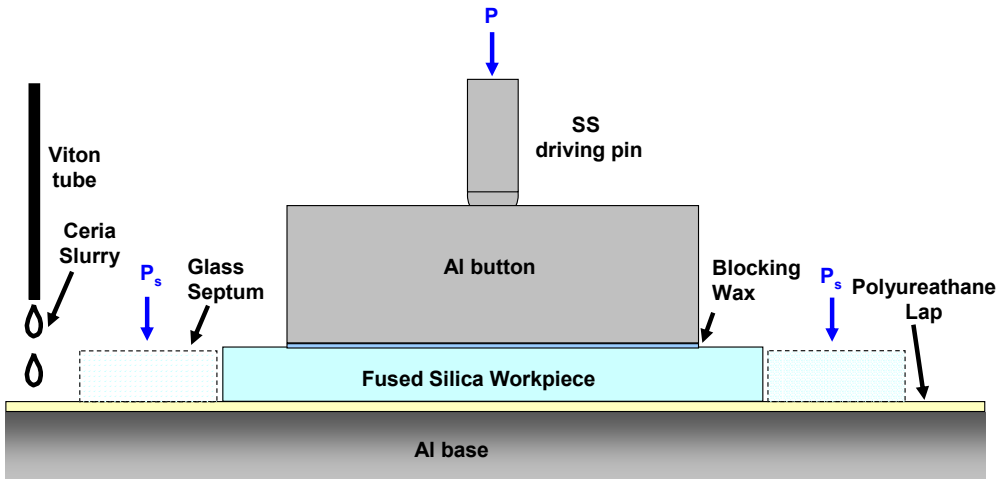

(a)

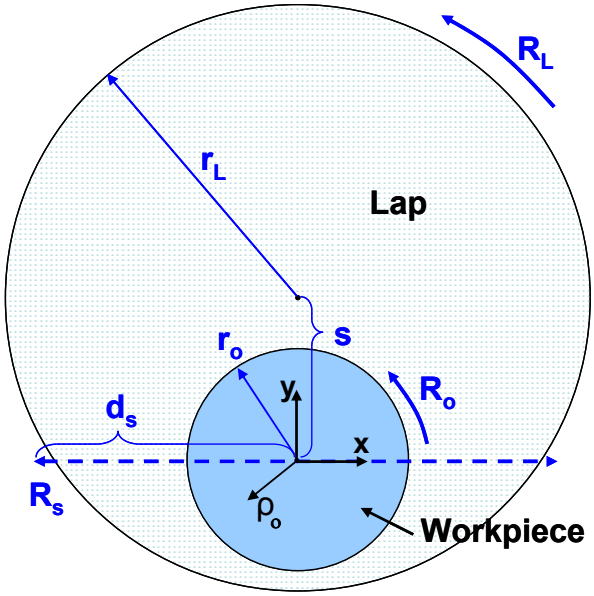

(b)

Figure 1. (a) Cross section view of the polisher configuration. (b) Top view schematic of polisher and workpiece illustrating kinematic degrees of freedom and coordinate system.

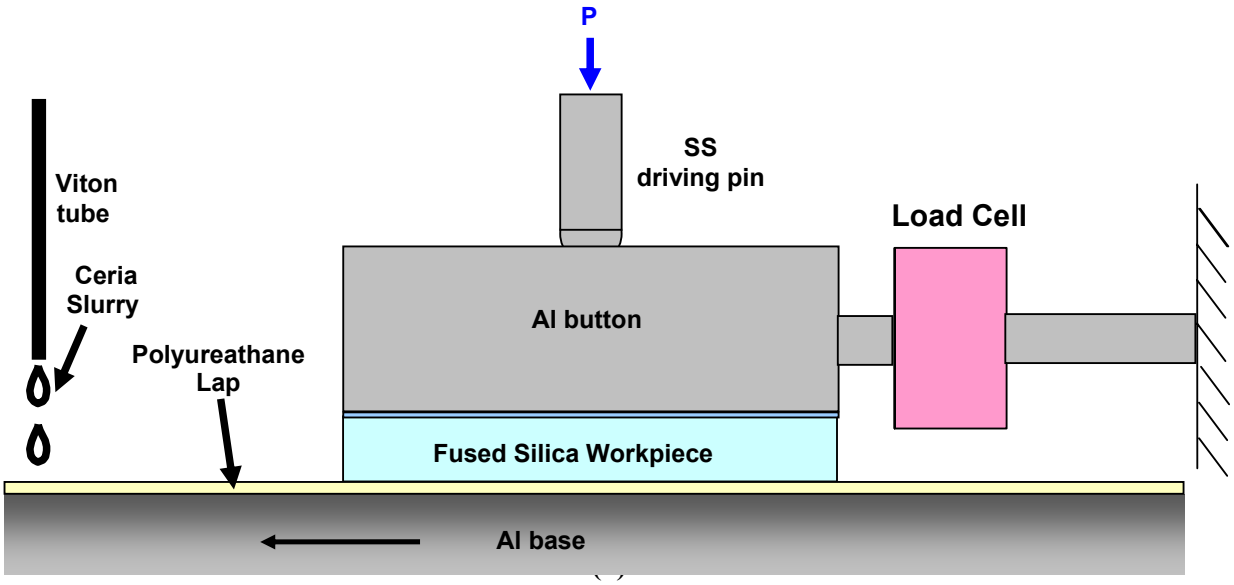
P
SS
driving pin
Viton
tube
Ceria
Slurry
Polyureathane
Lap
Load Cell
Al button
Fused Silica Workpiece
Al base

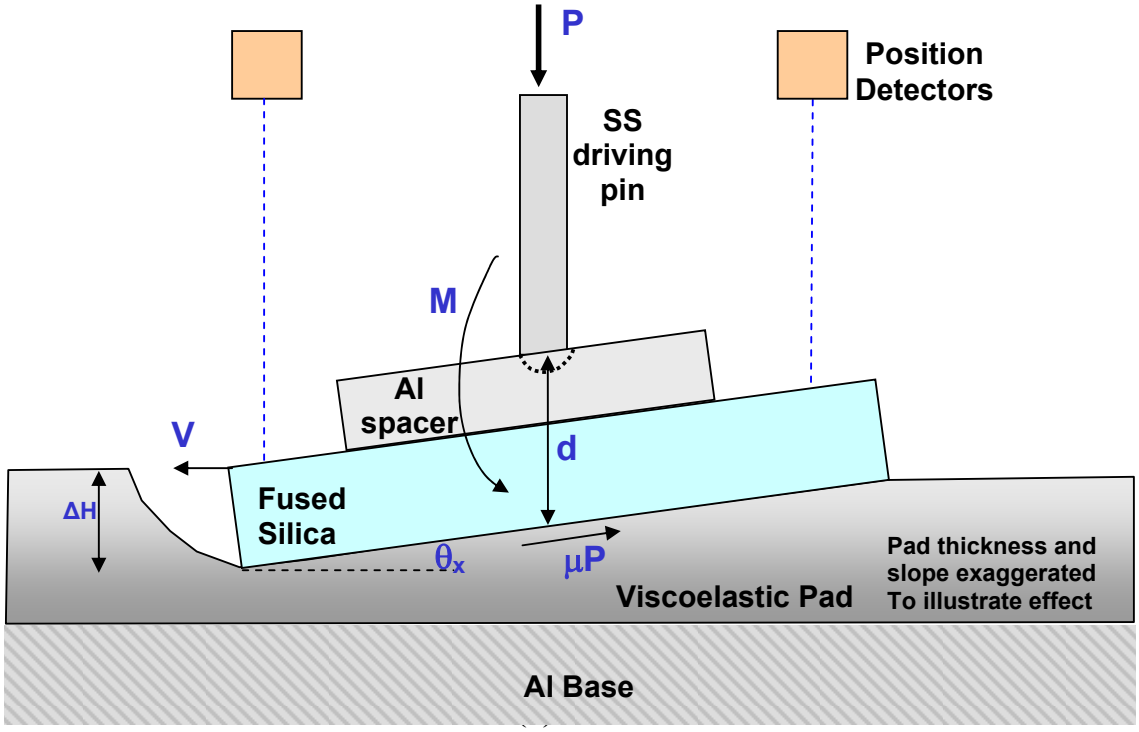
P
Position
Detectors
SS
driving
pin
M
Al
spacer
V
d
ΔH
Fused
Silica
θx
μP
Pad thickness and
slope exaggerated
To illustrate effect
Viscoelastic Pad
Al Base

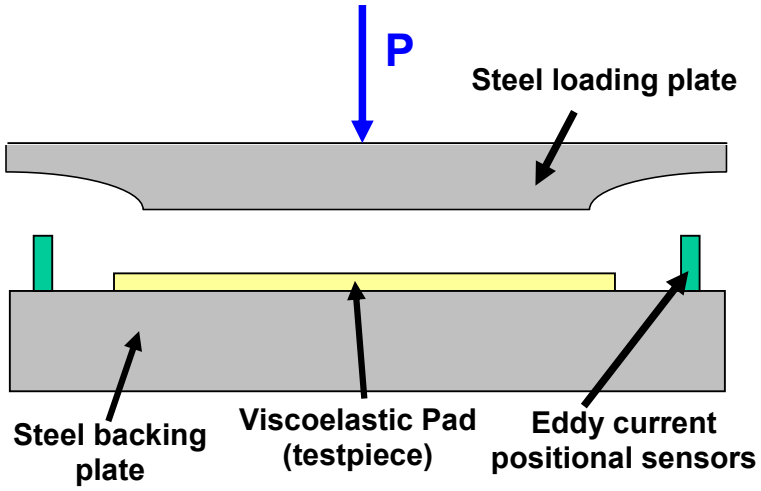

(c)

Figure 2: (a) Schematic of the setup used to measure the friction force on the lap as function of lap velocity and load (P); (b) Schematic of the setup used to measure the height difference and slope between the leading and trailing edge of the workpiece relative to the lap plane. (c) Schematic of the mechanical setup to measure the viscoelastic properties of the lap.

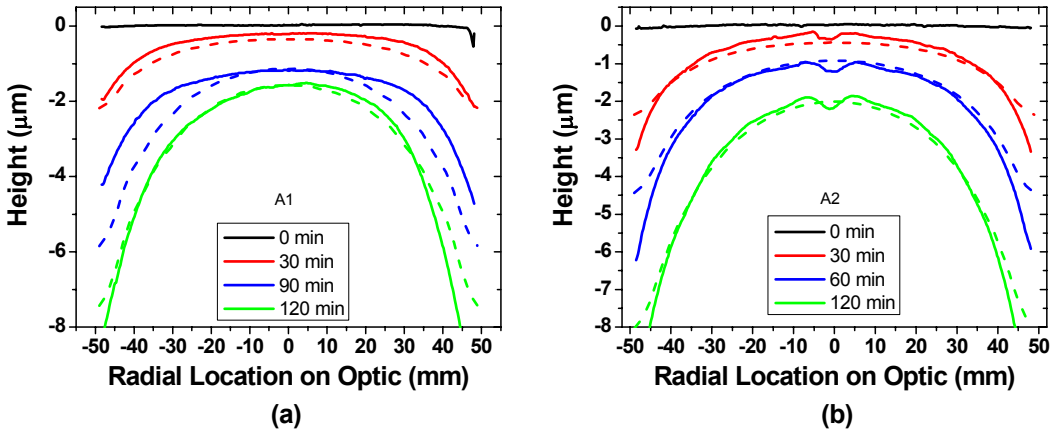

Figure 3: Baseline series radial surface profile of fused silica workpiece after polishing under different conditions [(a) Sample A1; (b) Sample A2] for various times. The solid line is the experimental data and the dashed line is the model fit using parameters described in Table 1.

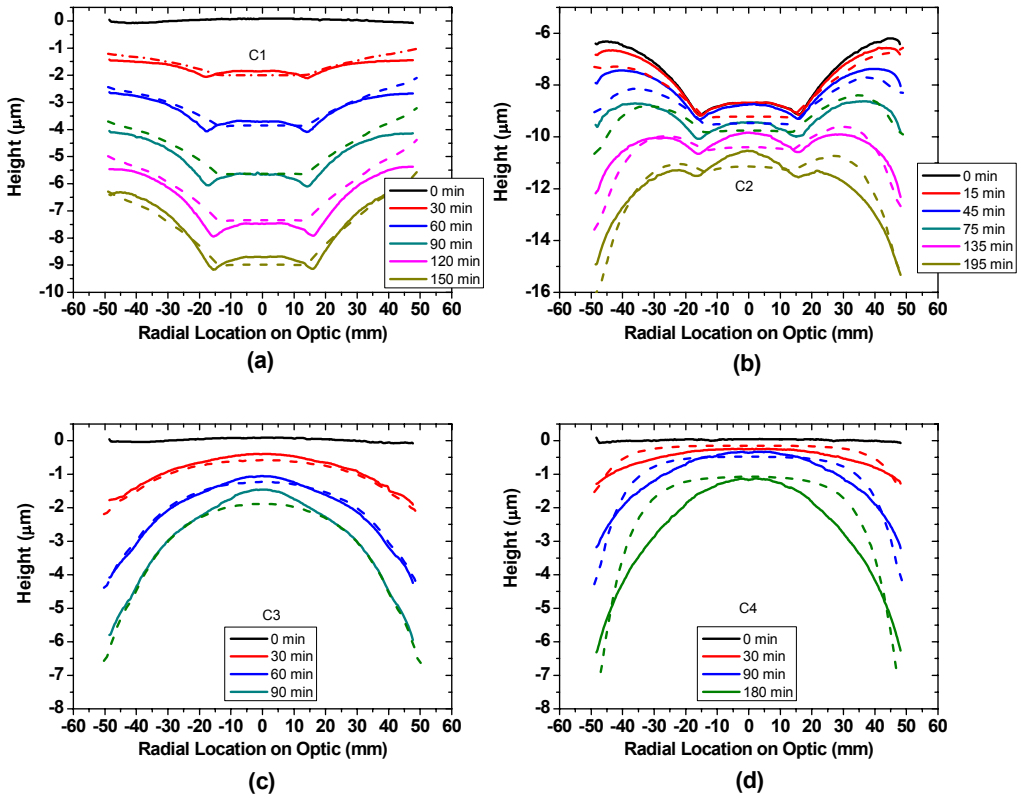

Figure 4: Flat lap series radial surface profile of fused silica workpiece after polishing under different conditions [(a) Sample C1; (b) Sample C2; (c) Sample C3 and (d) Sample C4] for various times. The solid line is the experimental data and the dashed line is the model fit using parameters described in Table 1.

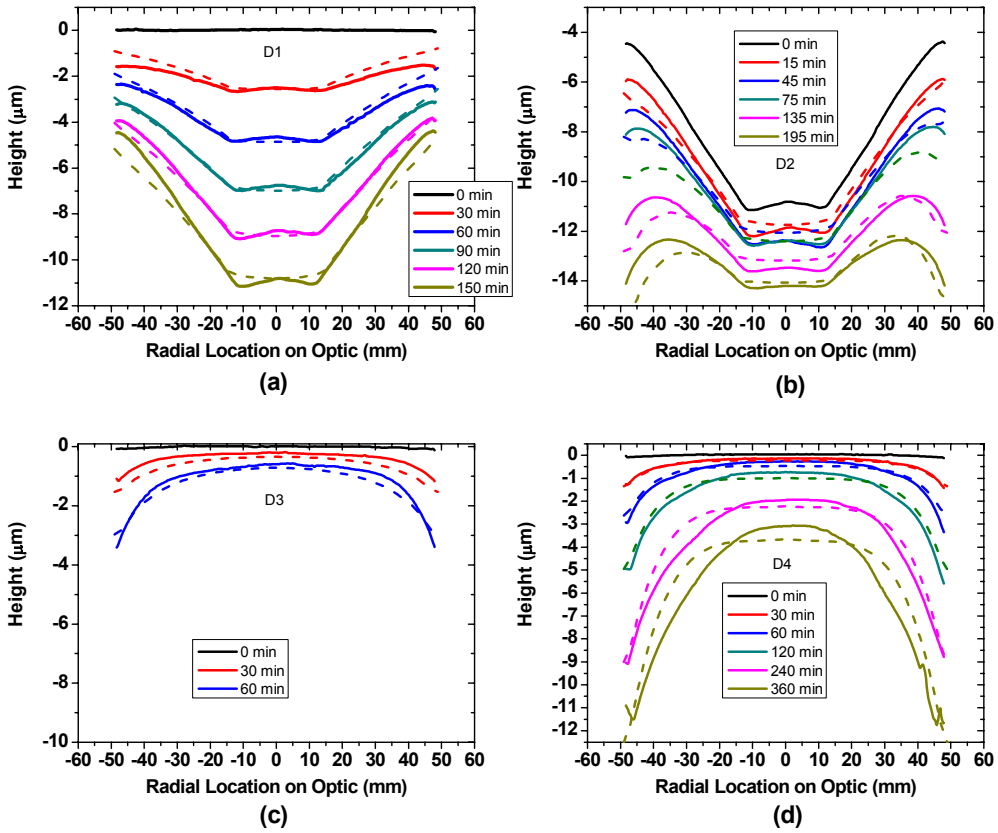

Figure 5: Curved lap series radial surface profile of fused silica workpiece after polishing under different conditions [(a) Sample D1; (b) Sample D2; (c) Sample D3 and (d) Sample D4] for various times. The solid line is the experimental data and the dashed line is the model fit using parameters described in Table 1. The polishing conditions are the same as shown in Fig. 4, but for a convex lap (peak-to-valley = 20 μm).

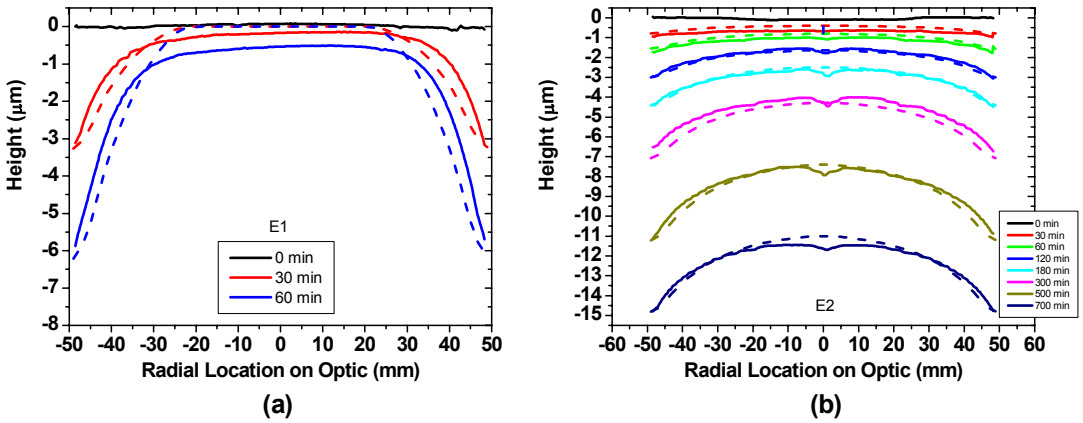

Figure 6: Loading series radial surface profile of fused silica workpiece after polishing under different conditions [(a) Sample E1; (b) Sample E2] for various times. The solid line is the experimental data and the dashed line is the model fit using parameters described in Table 1.

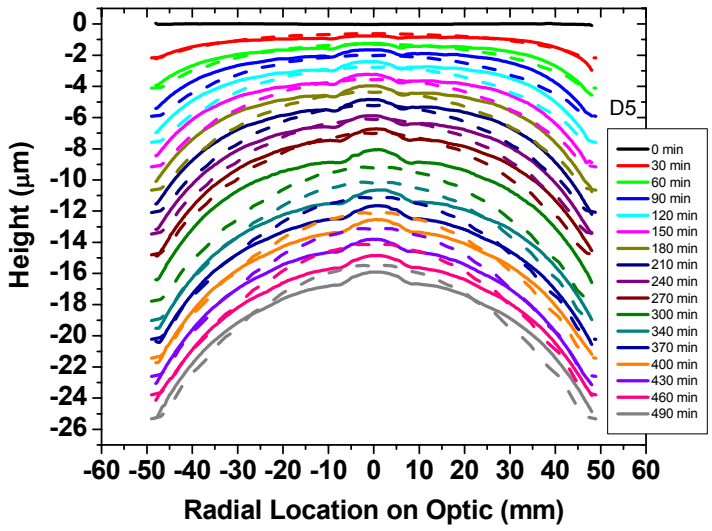

Figure 7: Radial surface profile of fused silica workpiece after polishing under conditions for Sample D5 for various times. The solid line is the experimental data and the dashed line is the model fit using parameters described in Table 1.

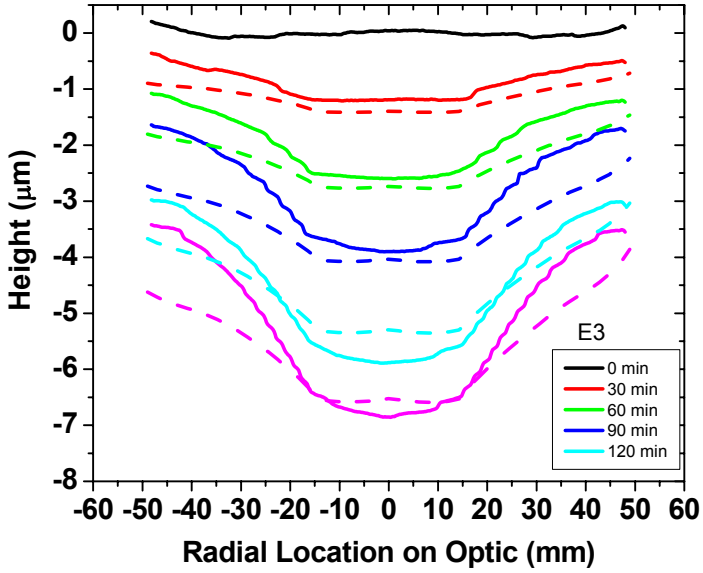

Figure 8: Radial surface profile of fused silica workpiece after polishing under conditions for Sample E3 for various times. The solid line is the experimental data and the dashed line is the model fit using parameters described in Table 1.

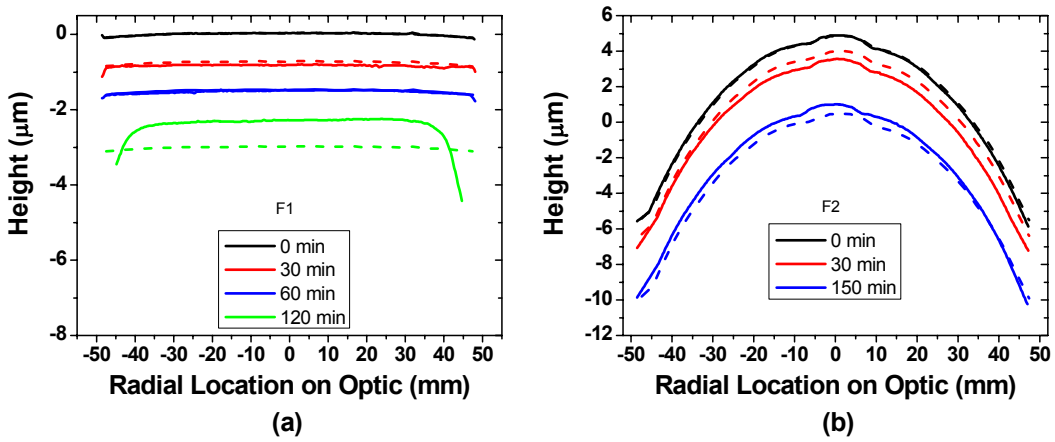

Figure 9: Septum series radial surface profile of fused silica workpiece after polishing under different conditions [(a) Sample F1; (b) Sample F2] for various times. The solid line is the experimental data and the dashed line is the model fit using parameters described in Table 1.

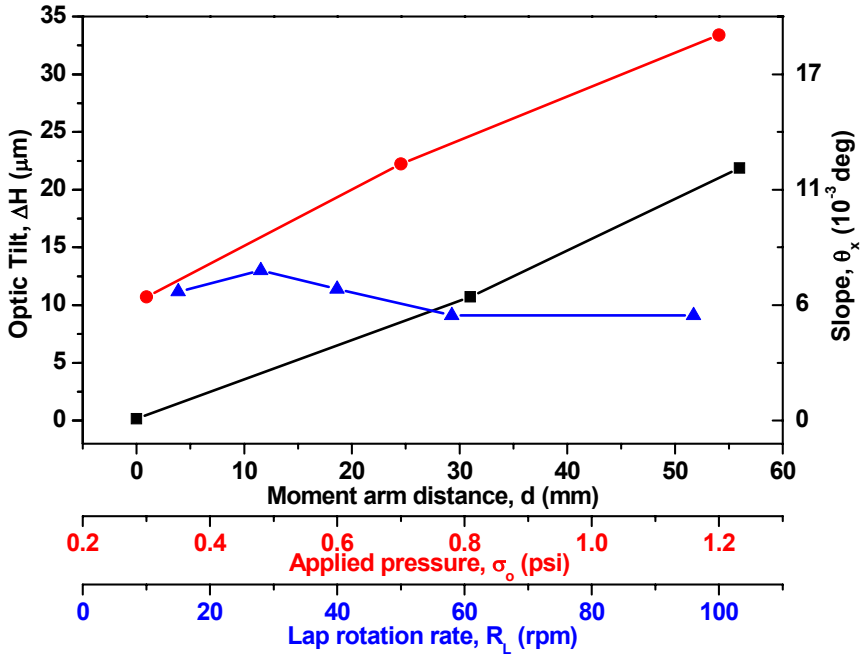

Figure 10: Measured workpiece tilt (ΔH) or slope as function of moment arm distance (d), applied pressure (σ_o), and lap rotation rate (R_L).

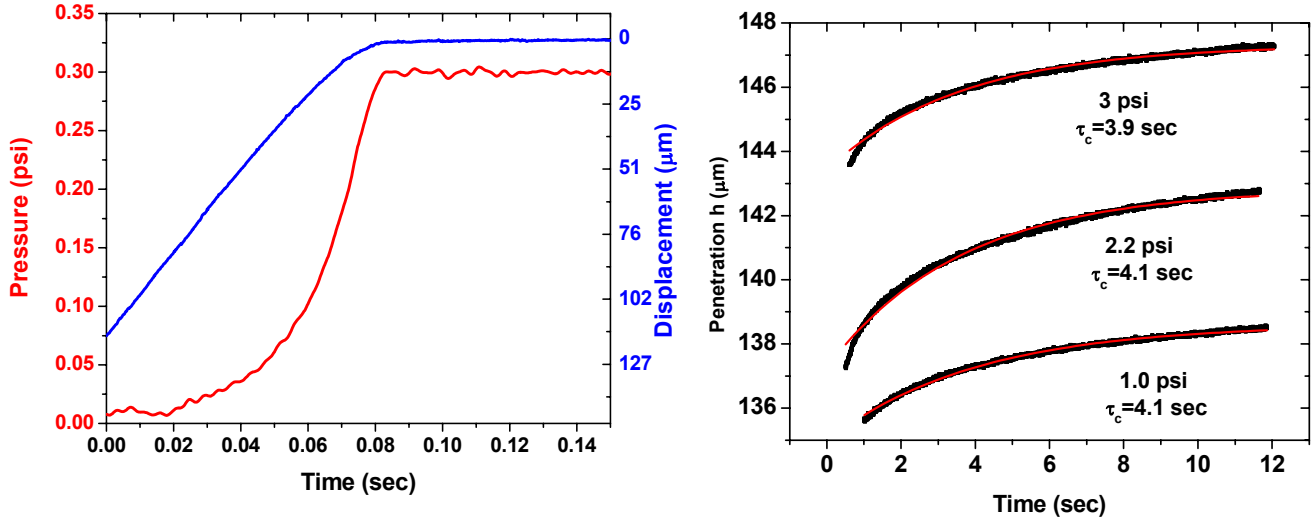

(a) (b)

Figure 11: (a) Measured pressure and displacement of the polyurethane polishing pad upon loading up to 0.33 psi using the setup described in Section 2.3; (b) Measured workpiece lap displacement using the setup described in Section 2.5 after full loading has been reached for various applied loads.

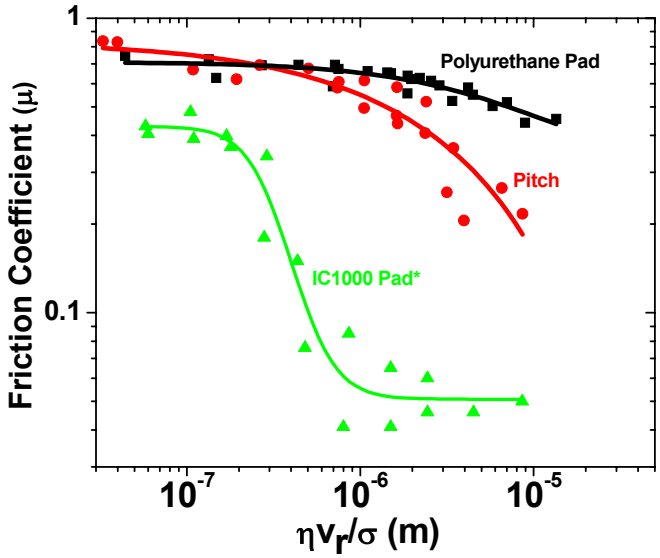

Figure 12: Measured friction coefficient as a function of applied pressure and relative velocity plotted in terms of the Stribeck curve. Polyurethane pad data and pitch data are from this study; IC1000 pad data are from [5]. Line represents a sigmoidal fit to the data for each lap material.

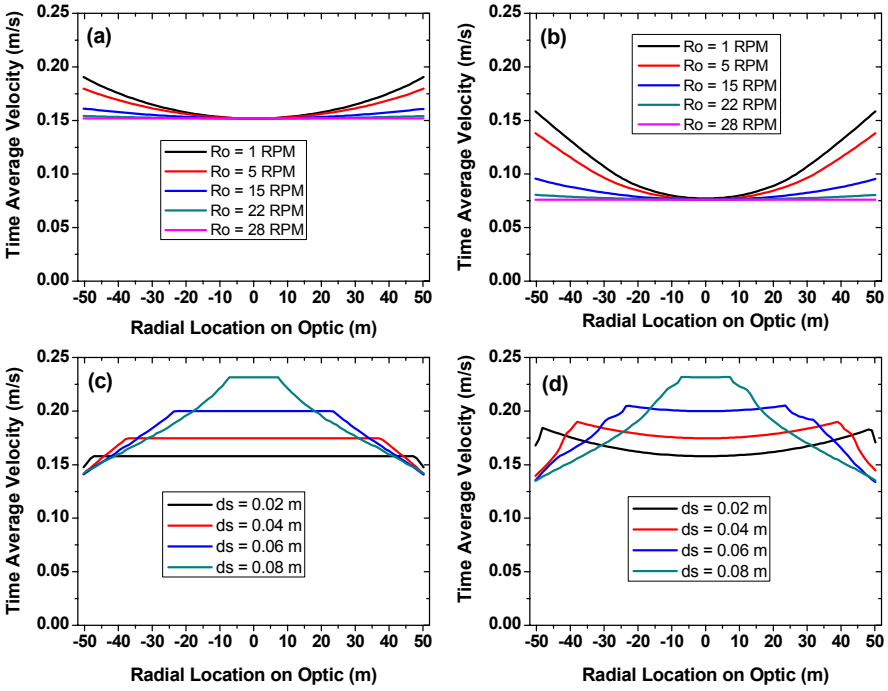

Figure 13. Calculated time averaged relative velocity using kinematic equations described using Eqs. 8-10 where r_o=0.05 m, r_L=0.1 m, R_L=28 rpm. (a) Effect of relative workpiece rotation rate with no stroke (s=0.025 m, R_s= 0 rpm, d_s= 0 m and R_o is varied); (b) Effect of relative workpiece rotation rate with larger separation distance (s=0.05 m, R_s= 0 rpm, d_s= 0 and R_o is varied); (c) Effect of stroke with workpiece/lap rotation matched (s=0.05, R_s= 15 rpm, R_o= 28 rpm, and d_s is variable); and (d) Effect of stroke with workpiece/lap rotation mismatch (s=0.05, R_s= 5 rpm, R_o= 15 rpm, and d_s is variable).

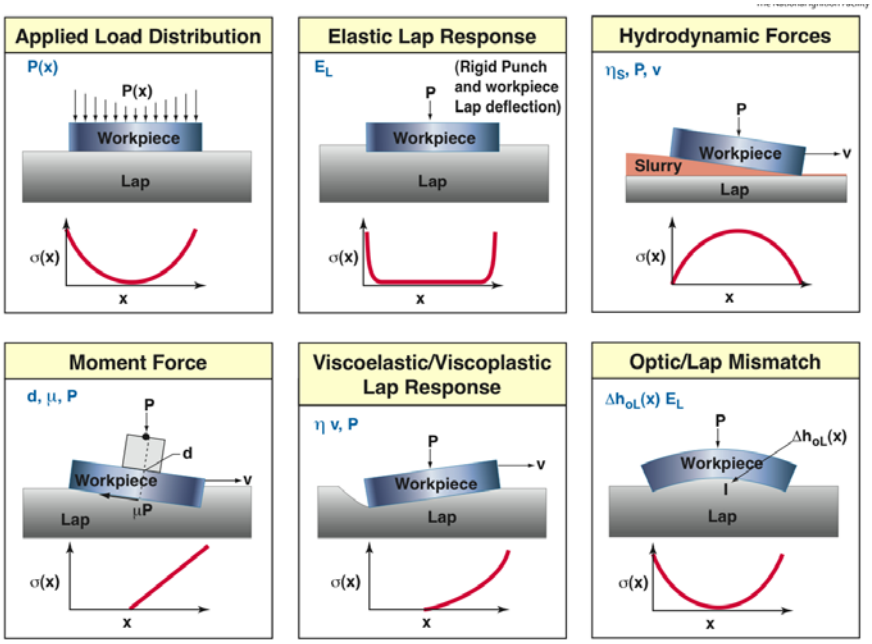

Figure 14: Schematic illustration of various physical effects that can contribution to the pressure distribution between a lap and workpiece. A typical shape for the pressure distribution is shown as well as identification of key process parameter that influence the pressure distribution.

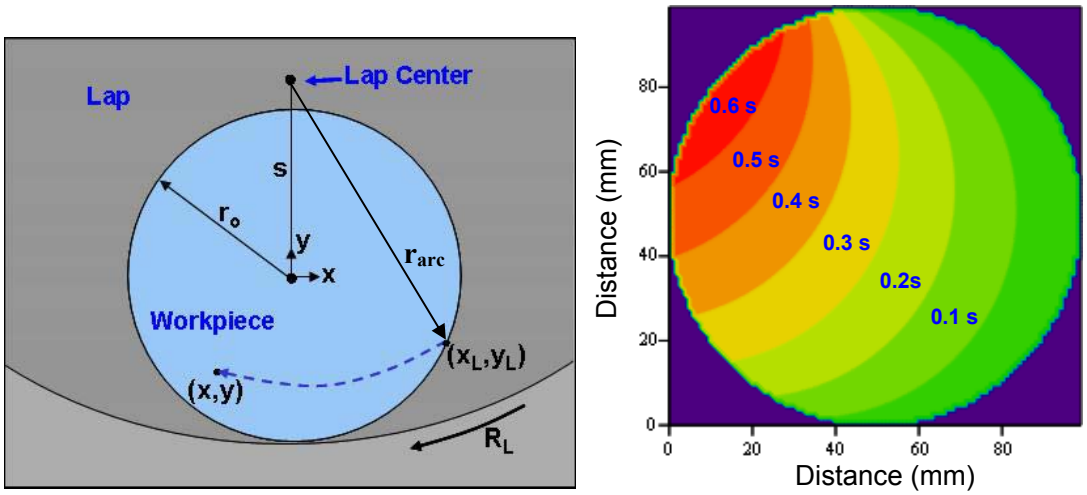

(a) **(b)**

Figure 15. a) Schematic illustrating a given point (x,y) on the workpiece at time $t_L(x,y)$ and the trace of the corresponding point on the lap while it was loaded starting at leading edge of workpiece at point (x_L, y_L). b) Contour plot of the calculated time of lap exposure for all points on the workpiece surface for the conditions (r_O = 0.05 m, R_L = 20 rpm, s = -0.075 m).

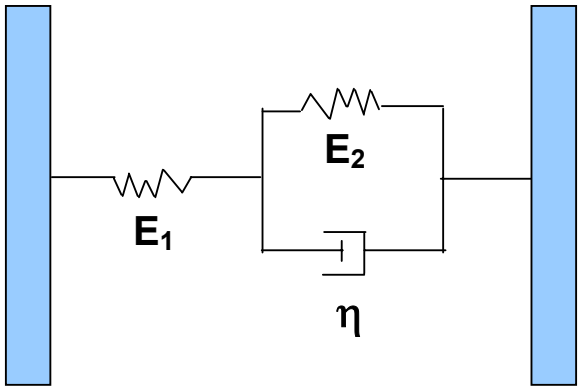

Figure 16: Schematic illustration of the delayed elasticity model to describe the viscoelastic behavior of a polyurethane polishing pad.

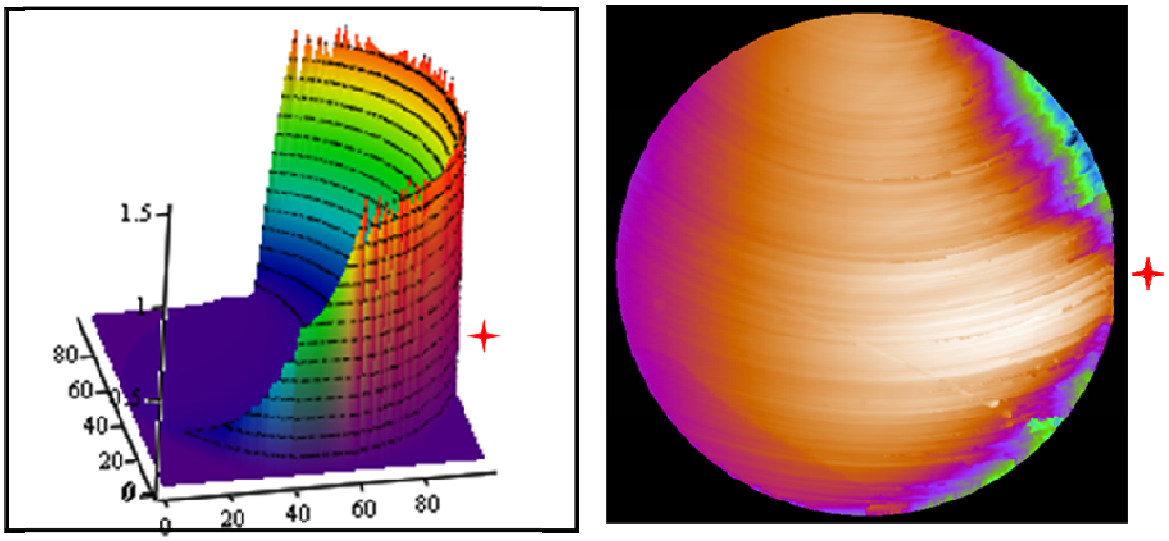

Figure 17: (a) Calculated stress profile conditions used for Sample B (non rotating workpiece) using Eqs. 13-18. (b) Measured surface profile for Sample B after 1 hour of polishing. Note that leading edge of the workpiece in each image is designated by a red star.

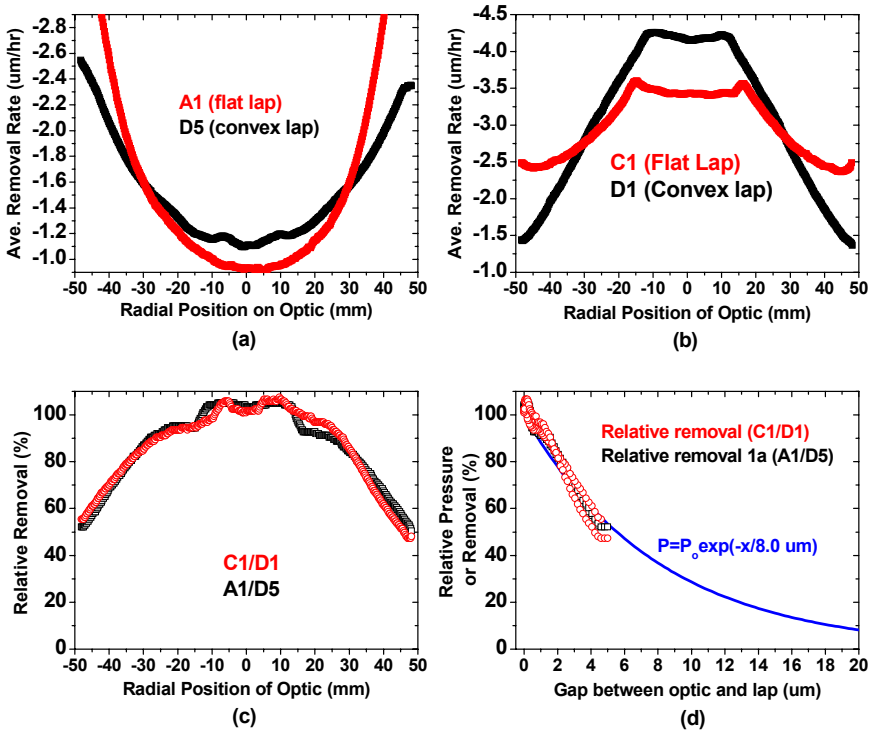

Figure 18: (a) Measured average removal rate for Samples A1 and F5 using a flat and convex lap respectively. (b) Measured average removal rate for Samples E1 and F5 using a flat and convex lap respectively. (c) Relative removal (normalized at center of workpiece) between flat and convex lap using measured average removal rate shown in (a) and (b). (d) Relative pressure or removal as a function of mismatch or gap between the contacting surface profiles between workpiece and lap (determined from the data in (c) and Eqs. 20-22). The solid line is a single exponential fit as described by Eq. 23.

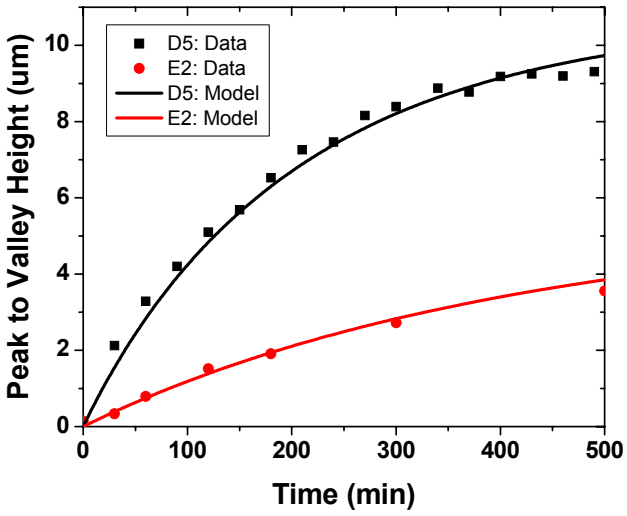

Figure 19: PV height of the surface figure for samples D5 & E2 as a function of polishing time. The points represent measured data and the line is the model simulation using SurF.

Variable List

d	Moment arm distance (m)
d_s	Stroke amplitude distance (m)
E_1,E_2	Moduli of viscoelastic lap for delayed elasticity model (Pa)
E	Bulk Modulus of lap (Pa)
$E_{rel}(t)$	Stress relaxation function of lap (Pa)
F	Frictional force between workpiece and lap (N)
F_x, F_y	Frictional force between workpiece and lap in x & y direction (N)
$\overline{h}$	workpiece/lap mismatch rate constant for drop in pressure with gap
h_i	Initial elastic displacement of lap under load (μm)
$h_L(x)$	Height of lap as a function of position (μm)
$h_o(x)$	Height of workpiece as a function of position (μm)
Δh	Overall height difference of surface of workpiece between polishing run iterations determined from interferometric lineouts (μm)
h_{PV}	peak-to-valley surface height of lap due to Al base curvature (μm)
$\Delta h_{oL}(x)$	Gap between workpiece and lap as a function of position (μm)
Δh_{oL}*	Gap between workpiece and lap where hydrodynamic pressure is maximum (μm
ΔH_f ,ΔH_r	Average measured height difference between leading edge and trailing edge of workpiece in forward (f) and reverse (r) direction (μm)
ΔH	Height difference between leading edge and trailing edge of workpiece relative to lap plane (μm)
$\frac{dh_i}{dt}$	Instantaneous material removal rate (μm/hr)
$\frac{dh}{dt}$	Average material removal rate (μm/hr)
$J(t)$	Creep compliance of lap (1/Pa)
k_p	Preston's constant for material removal (m^2/N)
$L(x,t_i)$	Measured radial profilometry height of optical surface as function of polishing time t_i
Mx, My	Moment between workpiece and lap in x & y direction (Nm)
Δm	Mass change of workpiece between polishing run increments (gm)
$\vec{R}_o$	Rotation rate of workpiece expressed in vector notation
$\vec{R}_L$	Rotation rate of lap expressed in vector notation
R_s	Stroke cycle rate
r_o	Radius of workpiece (m)
r_L	Radius of lap (m)
r_{arc}	Arc radius; distance from lap center to a given leading edge point on workpiece
P	Applied load on workpiece (N)
P_s	Applied load on septum (N)
s	Separation distance in y direction between center of workpiece and center of lap (m)
$\vec{S}$	Vector describing the separation between workpiece center and lap center (m)
t_{pad}	Initial thickness of pad (mm)
t	Polishing time (sec)
t_i	Polishing time increment (sec)
$t_L(x,y)$	Time of continual exposure of point on lap corresponding to given point on workpiece
$\vec{v}_r$	Relative velocity vector at a given position on workpiece relative to lap (m/s)
V_r	Magnitude of time average relative velocity (m/s)
(x,y)	point in system relative to workpiece frame of reference (m)

(x_L,y_L)	point in system relative to workpiece frame of reference at leading edge of workpiece (m)
ε_o	Baseline elastic strain of lap (unitless)
ε	Strain on lap at a given position/time (unitless)
$\dot{\varepsilon}$	Strain rate on lap (s^{-1})
η	Viscosity of lap (Pa-s)
η_s	Viscosity of slurry (Pa-s)
μ	Friction coefficient between workpiece and lap (unitless)
ρ_L	radius of curvature of lap surface
ρ	density of fused silica (gm/cm^3)
$\vec{\rho}_o$	Position on workpiece relative to workpiece center frame of reference (m)
σ	Stress/pressure distribution at a given position/time on workpiece (Pa)
σ_o	Applied stress on workpiece (Pa)
θ_x	slope of workpiece in x direction relative to lap plane (deg)
θ_y	slope of workpiece in y direction relative to lap plane (deg)
τ_c	Creep compliance time constant for lap (s)
τ_s	Stress relaxation time constant for lap (s)

Table 1: Summary of fused silica polishing samples

Series	Experiment	Experiment Conditions						Kinematic Conditions							Model Fit Param	
		Work piece Load	Septum Load	Initial Lap Shape (PV)	Initial Workpiece Shape (PV)	Moment Dist.	Loading	Lap Radius	Workpiece Radius	Lap Rot.	Workpiece Rot.	Stroke Rot.	Stroke Dist.	Sep Dist.	Work piece Slope[a] (10^{-5})	Prest on's Const. (10^{-13})
		(psi)	(psi)	(μm)	(μm)	d (mm)	--	r_L (m)	r_o (m)	R_L(rpm)	R_o(rpm)	R_s(rpm)	d_s (m)	S (m)	θ_x(deg)	k_p (m^2/N)
Base	A1	0.35	NA	<1	<0.1	31	Pin	0.10	0.05	-29	-26	0	0	0.05	0	17.8
	A2	0.35	NA	<1	<0.1	31	Pin	0.15	0.05	-20	-18	0	0	0.075	0	19.5
*	B	0.35	NA	<1	<0.1	31	Pin	0.15	0.05	-20	0	0	0	0.075	0	17.8
Flat Lap Series	C1	0.35	NA	<1	<0.1	31	Pin	0.10	0.05	-28	-23	15	0.07	0.05	6.9	13.8
	C2	0.35	NA	<1	3	31	Pin	0.10	0.05	-28	-23	15	0.04	0.025	0.3	16.7
	C3	0.35	NA	<1	<0.1	31	Pin	0.10	0.05	-28	-23	15	0.04	0.05	1.3	17.2
	C4	0.35	NA	<1	<0.1	31	Pin	0.10	0.05	-29	-27	15	0.01	0.025	0	17.2
Convex Lap Series	D1	0.35	NA	20	<0.1	31	Pin	0.10	0.05	-28	-23.5	15	0.07	0.05	6.9	13.8
	D2	0.35	NA	20	3	31	pin	0.10	0.05	-28	-26.8	15	0.04	0.025	0.3	17.9
	D3	0.35	NA	20	<0.1	31	pin	0.10	0.05	-29	-27.5	15	0.04	0.025	0	17.2
	D4	0.35	NA	20	<0.1	31	pin	0.10	0.05	-29	-27	15	0.01	0.025	0	17.2
	D5	0.35	NA	20	<0.1	31	pin	0.10	0.05	-29	-26	0	0	0.05	0	17.0
Loading Series	E1	0.35	NA	<1	<0.1	56	pin	0.15	0.05	-20	-22	0	0	0.075	-11.5	19.5
	E2	0.35	NA	<1	<0.1	0	wheel	0.15	0.05	-20	-13	0	0	0.075	4.3	9.4
	E3	0.35	NA	<1	<0.1	0	wheel	0.10	0.05	-28	-7	15	0.07	0.05	6.9	10.3
Septu m	F1	0.35	1.0	<1	<0.1	Na	pin	0.15	0.05	-20	-18	0	0	0.075	0	16.4
	F2	0.35	1.0	<1	3	Na	pin	0.10	0.05	-29	-26	0	0	0.05		16.4

*No workpiece rotation; (a) assumes initial displacement is 10 μm